



# Simulation of permeable surfaces using the pressure–velocity jump approach: A lamellar screen upstream of a ground-mounted obstacle

Mao Xu, Luca Patruno<sup>\*</sup>, Stefano de Miranda

DICAM, University of Bologna, Bologna, Italy

## ARTICLE INFO

### Keywords:

Computational wind engineering  
Porous elements  
Permeable surfaces  
Pressure jump  
Wind shields  
Lamellar screens

## ABSTRACT

Permeable surfaces are nowadays widely adopted in the construction industry, with applications ranging from wind shields for bridge decks to the external layer of permeable double skin facades. However, due to the large scale separation between the overall structure dimension and the size of the pores, their modelling in CFD simulations is still extremely challenging and over-simplified homogenized models are often used in practice. Inspired by previous studies, the authors recently proposed a generalization of the well-known pressure-jump approach which accounts for flow deflections, denoted as pressure–velocity jump, *PVJ*. In this study, the derivation of the *PVJ* approach is briefly recalled and contextualized in the existing literature. Then, we use *PVJ* to study the influence of a lamellar screen positioned upstream of a ground-mounted obstacle using 2D URANS. In particular, simulations are performed using the proposed *PVJ* approach and Explicit Models, *EM*, in which lamellae are explicitly modelled, for square and a rectangular obstacles. Results show a good agreement between *EM* and *PVJ* based models, confirming the high potential of the proposed technique.

## 1. Introduction

Permeable surfaces find numerous applications in the construction industry, ranging from wind shields used for bridge decks to the external layer of permeable double skin facades. Despite being their use usually limited to non-structural ancillary elements, they are well-known to play a fundamental role in the definition of the overall aerodynamic behaviour of structures exposed to the wind action.

In particular, the impact of wind barriers on the aerodynamic behaviour of bridge decks is widely recognized and has been examined in recent experimental studies, for instance, in [Kozmar et al. \(2014\)](#) and [Buljac et al. \(2017\)](#). Permeable barriers are also used to mitigate wind-blown sand and recent studies on such regard can be found in [Bruno et al. \(2018\)](#) and [Raffaele et al. \(2021\)](#). Another typical application of permeable surfaces is as cladding elements (see [Zhou and Chen \(2010\)](#) and [Pomaranzi et al. \(2021a\)](#)) or louvers (see [Packwood \(2000\)](#) and [Lo et al. \(2020\)](#)). A review paper analysing their use in the optimization of high-rise building performance can be found, for instance, in [Jafari and Alipour \(2021\)](#).

Despite being so widely and increasingly adopted, studying structures including the effects of porous surfaces poses several challenges for Wind Tunnel Tests, WTTs ([Allori et al., 2013](#); [Belloli et al., 2014](#)). In particular, in reduced-scaled WTT models, concerns are often raised regarding the actual representativeness of permeable elements, whose geometry cannot be simply scaled down like the rest of the model and

usually need to be simplified and modified to ensure manufacturability. This often requires to increase the thickness of the porous elements and modify the pores arrangement. As a result permeable elements adopted in WTTs are selected to match their full-scale aerodynamic resistance rather than their geometry, which might be anyway not representative of their full-scale behaviour due to the strong mismatch in Reynolds number. Additional problems derive from the impossibility to measure pressure distributions, if not for a few points, due to the lack of space to accommodate the piping system.

Regarding CFD simulations, reproducing the geometry considering all the pores, hereinafter denoted as Explicit Modelling *EM*, usually leads to prohibitive computational costs and models which are extremely cumbersome to set-up. In fact, *EM*, require to mesh in a sufficiently accurate way the elements composing the permeable barrier, leading to numerous small cells. The situation is further worsened by the fact that pores often induce velocity concentrations in correspondence of such small cells, which might impose to decrease the time step to guarantee the simulation stability, so sensibly increasing the computational costs.

To solve the problem, approaches based on homogenization techniques can be used, allowing to simulate the presence of permeable surfaces representing in a simplified way their interaction with the flow. Two main approaches are available to this purpose, namely the pressure-jump approach, *PJ*, and the use of porous media.

<sup>\*</sup> Corresponding author.

E-mail address: [luca.patruno@unibo.it](mailto:luca.patruno@unibo.it) (L. Patruno).

**Table of symbols**

$C_d$	Drag coefficient
$C_l$	Lift coefficient
$D$	Side length of the ground-mounted square
$F_d$	Drag force
$F_l$	Lift force
$L$	Distance between the lamellar screen and the ground-mounted square
$Re$	Reynolds number based on the distance between the elements of the lamellar screen
$U_{inlet}$	Inlet velocity magnitude
$\bar{U}$	Time-averaged velocity magnitude
$\bar{U}_y$	Time-averaged velocity vertical component
$c(\alpha)$	Coefficient that can be expressed means of a Fourier expansion
$\mathbf{u}$	Velocity vector upstream the permeable element
$\gamma$	Coefficiency to be calibrated
$\hat{u}$	Velocity versor
$\rho$	Fluid density
$b_{ni}, b_{ti}$	Model parameters where $i = 0, 1, etc$
$d$	Distance between the elements of the lamellar screen
$f_n$	Force per unit area exerted by the fluid on the permeable element along its normal direction
$f_t$	Force per unit area exerted by the fluid on the permeable element along its tangential direction
$p_i$	Pressure measured upstream the permeable element
$p_o$	Pressure measured downstream the permeable element
$q$	Dynamic pressure
$u_{ni}$	Velocity component in the normal direction upstream the permeable element
$u_{ti}$	Velocity component in the tangential direction upstream the permeable element
$u_{to}$	Velocity component in the tangential direction downstream the permeable element
EM	Explicit Model
PJ	Pressure Jump
PVJ	Pressure–Velocity Jump
URANS	Unsteady Reynolds-averaged Navier–Stokes
WTT	Wind Tunnel Test

Following the *PJ* approach, the presence of the porous surface is represented introducing a jump in the pressure value between the two sides of the permeable element, calculated according to the local velocity. It can be easily shown that this corresponds to accounting only for forces exchanged between the fluid and the permeable element along its normal direction, so disregarding the force tangential components. The value of the pressure-jump can be also related to the surface porosity and, eventually, the pore Reynolds number, relying on analytical and semi-analytical relations (Xu et al., 2020; Eckert and Pfluger, 1942; Taylor, 1944; Wieghardt, 1953). A review of these relations is reported in Azizi (2019). This approach has been widely adopted for modelling internal flows passing through nets and filters, while external aerodynamics problems have been rarely considered (see for instance Tominaga and Shirzadi, 2022; Xu et al., 2022c,a,b).

Alternatively, following the approach based on the use of porous media, the presence of the porous surfaces is represented by introducing a distributed resistance to the flow in a thin volume using the

Darcy–Forchheimer model (Darcy, 1856; Forchheimer, 1901), i.e. introducing a distribution of appropriately specified momentum sinks. As mentioned in Ooi et al. (2019) and Pomaranzi et al. (2021b), by using a full matrix to relate the local velocity to the momentum sinks, the approach is able to account for shearing effects. The method has as main drawback the need to define a thin porous zone which makes the case setup cumbersome and might be prone to numerical errors due to the reduced number of cells usually adopted along the permeable element thickness. Additionally, as for the *PJ* approach, the model is usually accurate for flows impinging the porous elements orthogonally, while accuracy decreases for flows impinging almost tangentially.

Inspired by the aforementioned works, the authors recently developed a generalization of the *PJ* approach, conceived to account for shearing effects and preserve a good accuracy for all flows incidence angles. It can be easily proved that shearing effects lead to jumps in the velocity tangential component and, thus, the model has been denoted as pressure–velocity jump approach, *PVJ*. The model has been successfully tested for the simple case of an isolated ground-mounted permeable barrier, proving its ability to reproduce flow patterns for barriers characterized by very different aerodynamic behaviour, ranging from perforated plates to lamellar screens with lamellae oriented in various directions (Xu et al., 2023). An OpenFOAM implementation of the method is freely available for download at <https://site.unibo.it/cwe-lamc/en>.

In this paper, we further investigate the accuracy of the *PVJ* approach for two-dimensional Unsteady Reynolds-averaged Navier–Stokes, URANS, models. To this purpose, we consider a ground-mounted permeable barrier composed of lamellae, located upstream of an obstacle at varying distance (both a square and a rectangular obstacle are considered). The study is aimed at assessing the accuracy of the obtained results against cumbersome *EM* and considerably extends the validation presented in Xu et al. (2023), considering cases in which the wake of the permeable element impinges on a bluff body. The case is conceived to be as simple as possible but still retain considerable technical value. In particular, within the well-known limitations of URANS models, for short distances between the permeable surface and the obstacle, the case is representative of configurations usually found when louvers (nowadays sometimes represented by solar panels) are positioned in front of building facades (please notice that the conclusions of this study shall not be automatically extrapolated to other model typologies as, for instance, those using scale resolving approaches to turbulence modelling).

The paper is organized as follows. In Section 2 a brief summary of the recently proposed *PVJ* approach is provided. Then, in Section 3 the test case is introduced and the settings adopted in the definition of the numerical model are detailed. Results obtained using *EM* and *PVJ* approaches are compared in Section 4. Finally, conclusions are drawn in Section 5.

## 2. The *PVJ* approach

The starting point of the *PVJ* approach is to define the pressure-jump and the tangential-velocity-jump according to the forces exchanged between the fluid and the permeable surface. In particular, with reference to Fig. 1, accounting for mass conservation and momentum conservation along the normal to the permeable surface, it can be easily shown that

$$p_o - p_i = -f_n, \quad (1)$$

being  $p$  pressure, the pedices  $i$  and  $o$  referring to values measured upstream and downstream the permeable element, respectively, and  $f_n$  the force per unit area exerted by the fluid on the permeable element along its normal direction. Analogously, considering momentum conservation along the tangential direction (we here consider only one tangential direction for the sake of simplicity), we obtain

$$u_{to} - u_{ti} = -\frac{f_t}{\rho u_{ni}}, \quad (2)$$

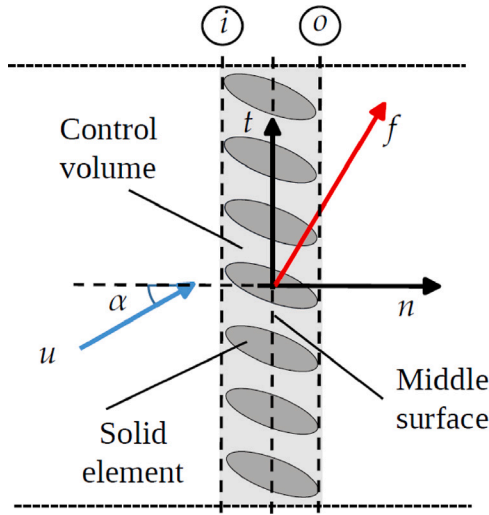


Fig. 1. Overview of a permeable element.  
Source: Image taken from Xu et al. (2023).

where  $u_t$  and  $u_n$  represent the velocity component in the tangential and normal direction, respectively,  $\rho$  is the fluid density and  $f_t$  is the force exerted by the fluid on the permeable element along its tangential direction.

Eqs. (1) and (2) allow to evaluate pressure and tangential-velocity-jumps when crossing the permeable element and require in input the aerodynamic forces for all incidence angles,  $\alpha$ . Following the approach adopted in Xu et al. (2023), aerodynamic forces are expressed as

$$f(\alpha) = \frac{1}{2} \rho |\mathbf{u}|^2 |\hat{\mathbf{u}}_n|^\gamma c(\alpha), \quad (3)$$

being  $\mathbf{f}(\alpha) = [f_n(\alpha), f_t(\alpha)]$ ,  $\mathbf{u}$  the upstream velocity vector  $\mathbf{u} = [u_n, u_t]$ ,  $\hat{\mathbf{u}}$  the velocity versor  $\mathbf{u}/|\mathbf{u}|$ ,  $\gamma$  a coefficient to be calibrated. The coefficients  $c(\alpha)$  can be conveniently expressed by means of a Fourier expansion

$$c(\alpha) = \begin{bmatrix} c_n \\ c_t \end{bmatrix} = \begin{bmatrix} b_{n0} + b_{n1} \cos(\alpha) + b_{n2} \sin(\alpha) + b_{n3} \cos(2\alpha) + b_{n4} \sin(2\alpha) \dots \\ b_{t0} + b_{t1} \cos(\alpha) + b_{t2} \sin(\alpha) + b_{t3} \cos(2\alpha) + b_{t4} \sin(2\alpha) \dots \end{bmatrix}, \quad (4)$$

in which  $b_{n0}$ ,  $b_{t0}$ ,  $b_{n1}$ ,  $b_{t1}$ , etc.. are model parameters which can be obtained from data fitting or, for some cases, analytically.

In particular, for the case of closely spaces lamellar screens, the lamellae impose a kinematic constraint to the outgoing flow, forcing it to be tangential to the lamellae. It is thus possible to demonstrate that

$$\mathbf{f} = \frac{1}{2} \rho |\mathbf{u}|^2 |\hat{\mathbf{u}}_n| \begin{bmatrix} 2 \tan^2(\theta) & -2 \tan(\theta) \\ -2 \tan(\theta) & 2 \end{bmatrix} \begin{bmatrix} \hat{\mathbf{u}}_n \\ \hat{\mathbf{u}}_t \end{bmatrix} \quad (5)$$

being  $\theta$  the angle between the lamellae tangential direction and the permeable surface normal direction. It can be easily seen that Eq. (5) is a particular case of Eq. (4) when  $b_{n0} = b_{t0} = 0$  and the expansion is truncated at the first harmonic. The interested reader is invited to refer to Xu et al. (2023) for further details.

### 3. Numerical model

As anticipated, in this study we consider a ground mounted lamellar screen positioned upstream of an obstacle. The obstacle is a square of side length  $D$  (see Fig. 2(a)). Overall the considered computational domain measures  $80D$  in the along wind direction and has a height of  $50D$ , resulting in a blockage ratio of 2.0%. The distance  $L$  between the lamellar screen and the obstacle is systematically varied, so that  $L/D$  is equal to 3.0, 2.0, 1.0, 0.7, 0.5, 0.3, and 0.1.

Two configurations of the lamellar screen are considered, corresponding to orientations of the lamellae which deflect the flow of 45 degrees upward and downward, respectively. In the following, those will be denoted as  $B-45$  and  $B+45$ , respectively (see Fig. 2(b) and (c)). As it can be seen in the aforementioned figure, lamellae are closely spaced, being their chord equal to  $D/9$  and their spacing equal to  $d = D/18$ .

Numerical simulations are performed adopting the well-known URANS  $k-\omega$  SST turbulence model (Menter et al., 2003). As regard boundary conditions, for pressure null gradient is prescribed at the inlet and zero pressure is imposed at the outlet. For velocity, a fixed velocity value,  $U_{inlet}$ , is imposed at the inlet boundary, while a zero-gradient boundary condition is imposed at the outlet. Values for  $k$  and  $\omega$  are imposed assuming a 1% turbulence intensity and a turbulent viscosity ratio equal to 2 at the inflow, while null gradient is imposed at the outlet. Symmetry conditions are imposed at the top of domain, while wall-functions are used for the bottom of the domain, the obstacle and the lamellae. A centred second-order differentiation scheme is adopted for the diffusive terms, while for non-linear advective terms, the Linear-Upwind Stabilised Transport (LUST) scheme is used (Weller, 2012). Time integration is performed using the Crank–Nicolson scheme and the time step is selected to make the maximum Courant number approximately equal to 1.0. The coupling of pressure and velocity is obtained using the well-known Pressure-Implicit with Splitting of Operators (PISO) algorithm.

Simulations are run for 200 non-dimensional time units,  $D/U_{inlet}$  and data used for postprocessing are extracted from the last 100 non-dimensional time units. The open-source Finite Volume software OpenFOAM® v2112 is used.

We here remark that the Reynolds number based on  $d$  and  $U_{inlet}$  is approximately equals to  $5.6 \times 10^5$ , a value for which results reported in Xu et al. (2023) show that the aerodynamic behaviour of the barrier is not prone to Reynolds effects (no effect was found in the range  $Re = 1.0 \times 10^4$  to  $1.0 \times 10^6$ ). Additionally, to ensure mesh independence, the mesh resolution here adopted is chosen in agreement with Xu et al. (2023), where 32 cells are used along each lamella chord. Employing this cell size results in a total of approximately 200k cells. On overview of the mesh is shown in Fig. 3(a), while close ups of the zone near the lamellar screen is shown in 3(b) and (c).

The model settings presented up to now are those adopted for the EM case, which is used as reference in the present study. The same settings are kept identical for the cases in which the lamellar screen is modelled using the PVJ approach. The only difference is that, using the PVJ approach, the lamellae are not represented explicitly and the permeable element is represented only by its middle plane, which in two-dimensions corresponds to the line passing through the centres of the lamellae.

In order to adopt the PVJ approach, the forces exchanged between the fluid and the permeable element shall be characterized considering all incidence angle. To this purpose the analytical formulation reported in Eq. (5) can be adopted. However, despite being able to capture the exchanged forces quite accurately, such formula does not account for flow detachments from the lamellae, which can lead to deviations between its predictions and measured forces. In this paper, we thus proceed adopting the calibration of the coefficients appearing in Eq. (4), presented in Xu et al. (2023). The calibration is performed considering an isolated elementary portion of the barrier in period conditions (see Xu et al. (2023) for details). For the sake of comparability, the mesh used to represent the lamellae for such calibration is substantially identical to the one here adopted for the EM model.

### 4. Results

In this section, we proceed to compare the results obtained from for the EM and PVJ models, where the former approach is considered as a reference to evaluate the performance of the latter one. Firstly, a detailed discussion of the results obtained for a square obstacle is presented. Then the results obtained for the rectangular obstacle are shown.



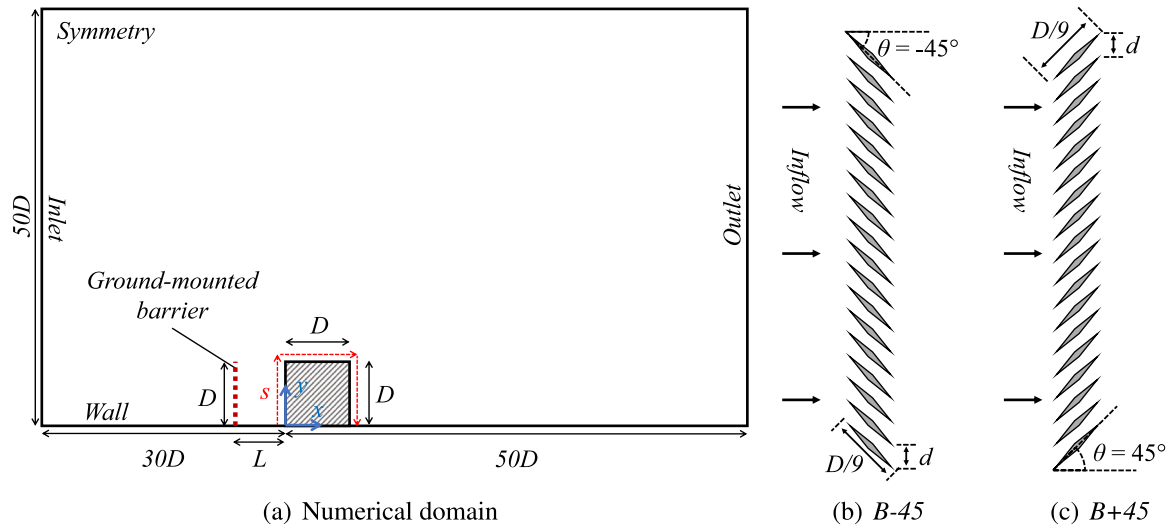


Fig. 2. Overview of the studied cases.

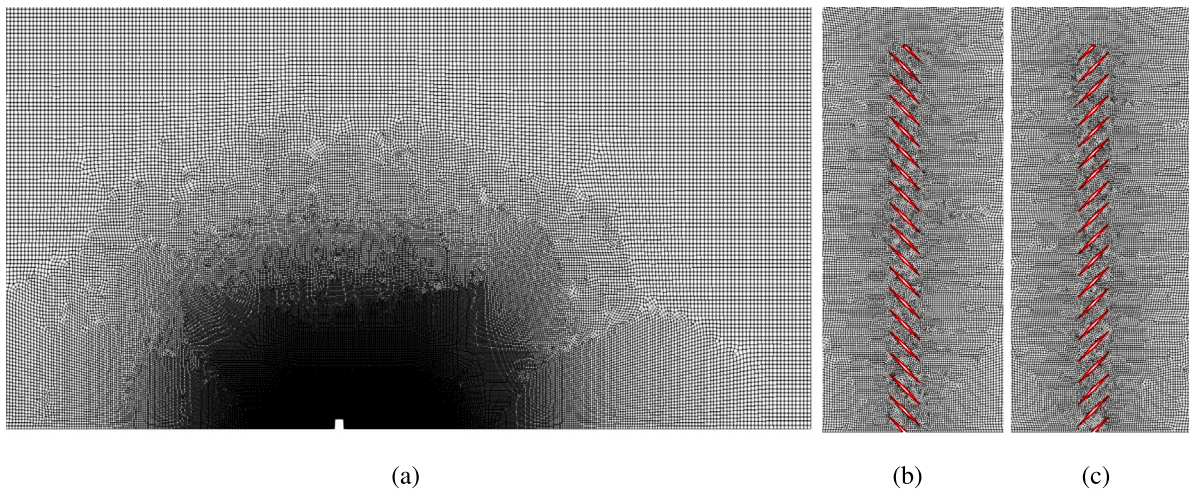


Fig. 3. The adopted mesh: (a) overall domain, (b) permeable barrier for  $B-45$  and (c) permeable barrier for  $B+45$ .

#### 4.1. Overall flow organization

We start the comparison between *EM* and *PVJ* models for the case of a square obstacle by inspecting the streamlines of the time-averaged velocity field, shown in Fig. 4 for  $B-45$  and in Fig. 5 for  $B+45$ . For the sake of conciseness, only the cases with  $L/D = 3.0, 1.0$  and  $0.1$  are here reported. Comparing such two figures, it can be seen that the orientation of the lamellae, as expected, has a great effect on the overall flow organization. The structure of the major vortical structures is well reproduced by *PVJ* in all cases. In general, differences appear to be more pronounced for the  $B+45$  cases when the distance  $L \geq D$ . Such differences appear to be quite limited in the zone between the lamellar screen and the obstacle, but lead to remarkable differences in its wake.

We now analyse the distribution of the time-averaged velocity. The contours of the time-averaged velocity magnitude,  $\bar{U}$ , are reported in Figs. 6 and 7, respectively. The figures further emphasize the good agreement between the *EM* and *PVJ* models for all cases, even those in which the lamellar screen is very close to the obstacle. The result is worth noticing as such conditions substantially differ from those used to calibrate the *PVJ* model (i.e. an elementary barrier element in periodic conditions with no wall in its proximity).

#### 4.2. Velocity profiles

Figs. 8 and 9 report profiles of the velocity magnitude in terms of  $\bar{U}/U_{inlet}$ , measured downstream the permeable barrier at  $x/d = 1$  and  $x/d = 5$  along vertical paths starting from the ground. As expected, results once again point to a good agreement between *EM* and *PVJ* models for all cases. Notice that the jiggling observed in the profiles measured at  $x/d = 1$  for *EM* are due to the presence of the solid elements composing the lamellae and quickly fade away proceeding downstream the barrier.

Similarly, Figs. 10 and 11 report profiles of the time-averaged vertical velocity component,  $\bar{U}_y/U_{inlet}$ , further emphasizing the differences induced by the inclination of the lamellae for the two considered cases,  $B-45$  and  $B+45$ , respectively.

#### 4.3. Aerodynamic forces

We now proceed to analyse the forces induced by the flow on the lamellar screen and the obstacle. Drag and lift forces are indicated as  $F_d$  and  $F_l$ , respectively, and aerodynamic coefficients are defined as  $C_d = F_d/qD$  and  $C_l = F_l/qD$ , where  $q = 1/2\rho U_{inlet}^2$ . Fig. 12 reports the aerodynamic coefficients measured on the lamellar screen for all

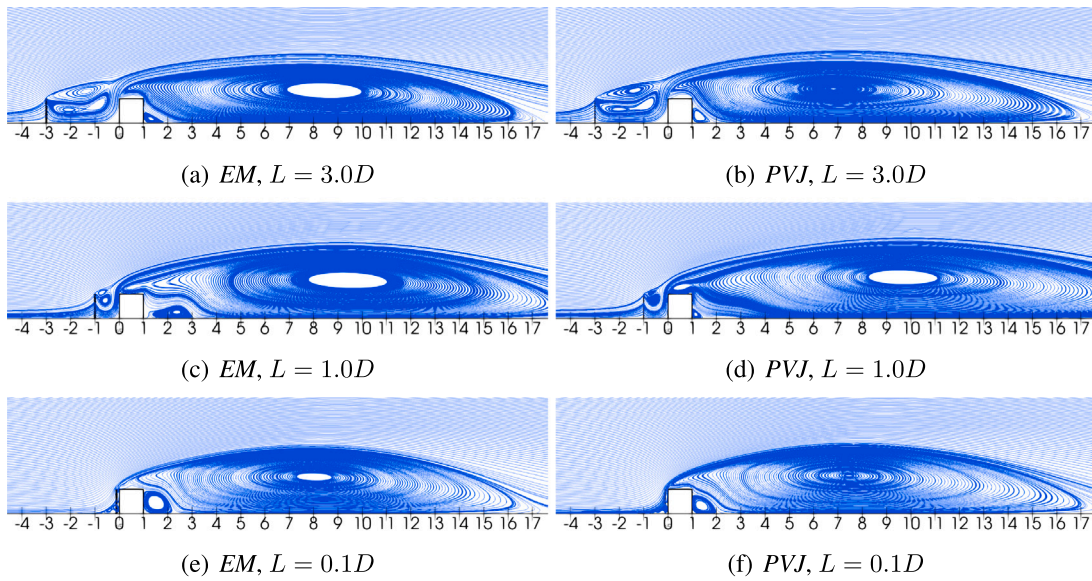


Fig. 4. Streamlines of the time-averaged velocity field for the *B-45* barrier.

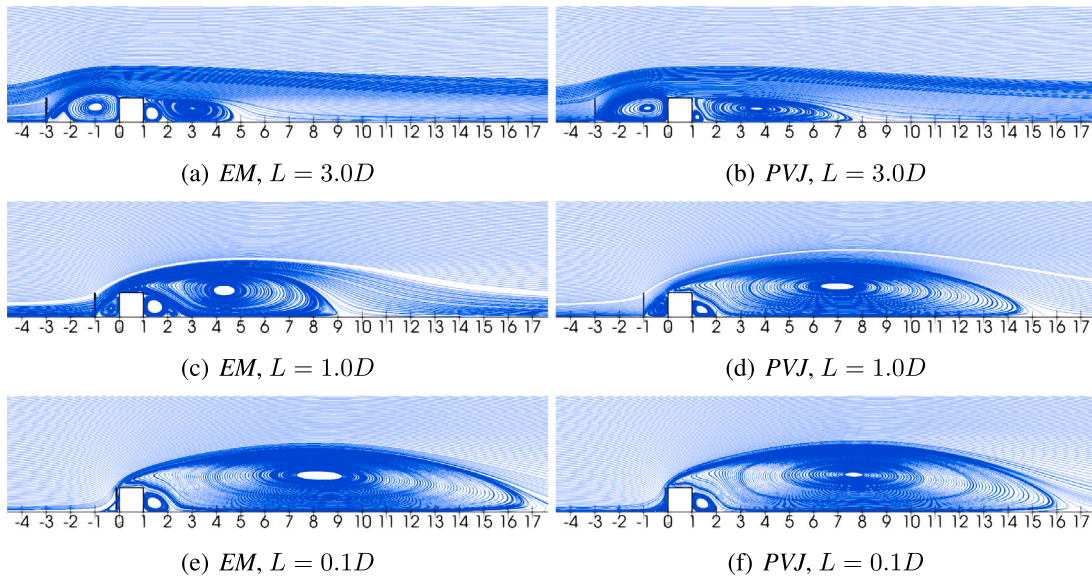


Fig. 5. Streamlines of the time-averaged velocity field for the *B+45* barrier.

the previously considered cases. Forces calculated using the *EM* and the *PVJ* approach appear to be in good agreement in all cases, with trends always well-reproduced. It is worth to notice that variations in the aerodynamic forces mainly occurs for  $0 < L < 1D$  and tend to stabilize for higher values of  $L$ , as expected.

Percent differences of the aerodynamic forces obtained using *EM* and *PVJ* models are reported in Fig. 13. In general, differences are in the order of 10%–20% for  $L \geq 0.3D$ . For cases characterized by  $L \leq 0.3D$ , noticeable percent differences are obtained but it shall be noticed that absolute values are quite small.

We now proceed to assess the accuracy of the obtained results in terms of the aerodynamic forces measured on the square obstacle immersed in the lamellar screen wake. In particular, in Fig. 14, *EM* and *PVJ* are compared in terms of the drag and lift coefficients exerted on the obstacle. As expected, in the case in which the flow is deflected in the direction of the ground (i.e. *B-45*), higher drag is observed due to velocity intensification at the stagnation point, together with a slow decrease as  $L/D$  increases. When the flow is deflected away from the ground (i.e. *B+45*), negative drag values are predicted for  $L > D$  which

quickly turn into positive ones when  $L$  is reduced and the lamellar screen is unable to deflect the flow from the obstacle.

For the sake of completeness, the differences of the forces measured on the immersed obstacle considering the *EM* and *PVJ* models are reported in Fig. 15. Values are mostly less than 20%, with some larger discrepancies found for  $C_l$  when  $L > D$ .

Finally, time-averaged pressure distributions along the path depicted in Fig. 2, are reported in Figs. 16 and 17 for the cases  $L = 0.1D$  and  $L = 3D$ , respectively. Again, while showing some inaccuracies in quantitative terms, results obtained with *EM* and *PVJ* models are in good qualitative agreement.

#### 4.4. Rectangular obstacle

To further investigate the performance of the *PVJ* approach, a rectangular obstacle is here considered, with aspect ratio 4:1. All numerical setups are identical to those previously adopted. According to the previously presented cases (based on a square obstacle) differences



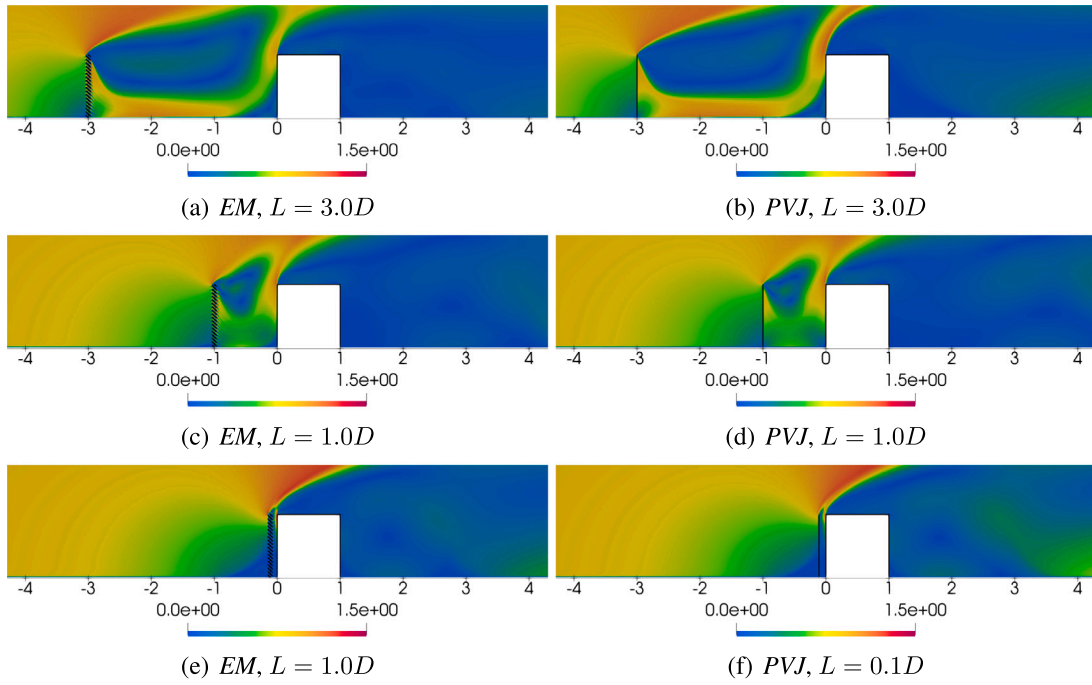


Fig. 6. Time-averaged velocity magnitude distribution,  $\bar{U}/U_{inlet}$ , for the B-45 barrier.

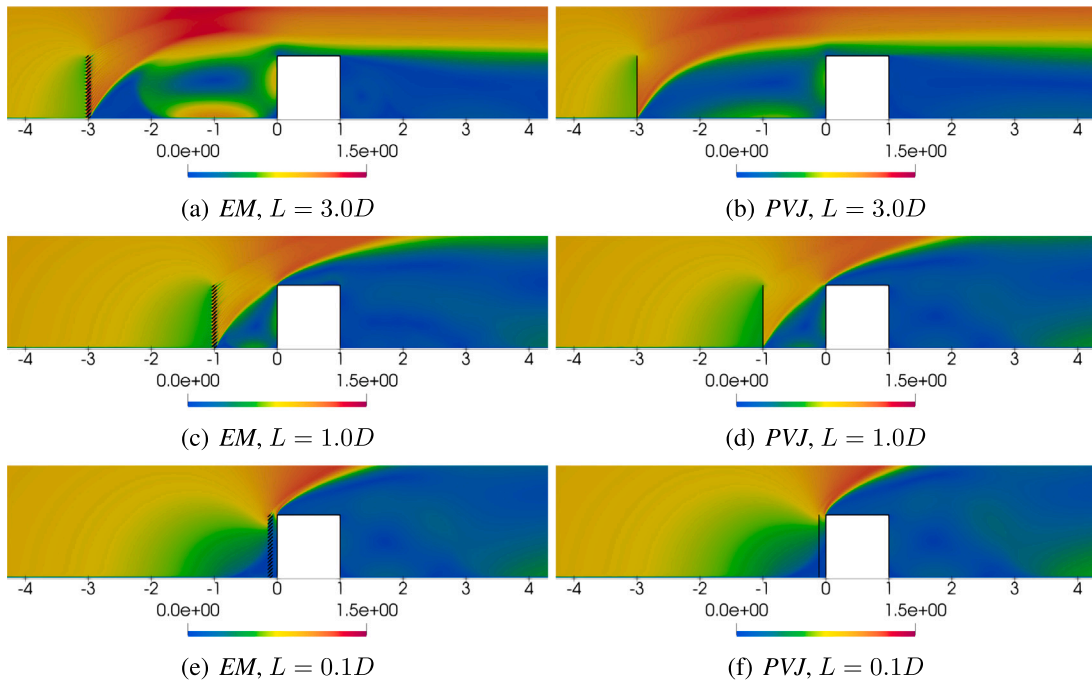


Fig. 7. Time-averaged velocity magnitude distribution,  $\bar{U}/U_{inlet}$ , for the B+45 barrier.

between EM and PVJ can be noticed especially when  $L \geq D$ . We thus here consider the case  $L/D = 1.0$ . Firstly, the time-averaged streamlines are shown in Fig. 18(a) for the case B-45. In this case good agreement is found between EM and PVJ models. Despite being the flow deflected down by the lamellar screen, no reattachment is predicted by both EM and PVJ models. On the contrary, for the case B+45, shown in Fig. 19(b), remarkable differences are recorded in the wake zone and the flow, which is deflected upward by the lamellar screen, tends to reattach on the obstacle upper part, although in an incomplete way.

Figs. 20 and 21 show the velocity field in the zone between the lamellar screen and the obstacle for the four analysed cases. It can

be seen that the agreement in such zone is very good and, thus, the differences previously discussed must arise due to downstream amplification of small mismatches developed in such area. In particular, Fig. 21 shows that the high velocity zone of the flow downstream the lamellar screen B+45 impinges the obstacle right at the corner, so representing a particularly delicate condition, especially when a long after-body which allows for reattachment is present.

Despite the aforementioned differences, the overall forces acting on the body and the lamellar screen appear to be in reasonably good agreement, arriving to 20% for the  $Cl$  of the B+45 case delicate case, as

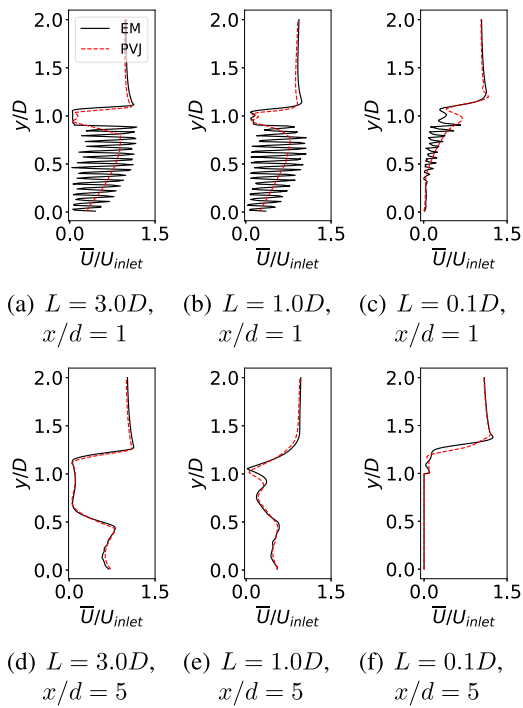


Fig. 8. Vertical profiles of time-averaged velocity magnitude,  $\bar{U}/U_{inlet}$ , downstream the B-45 barriers.

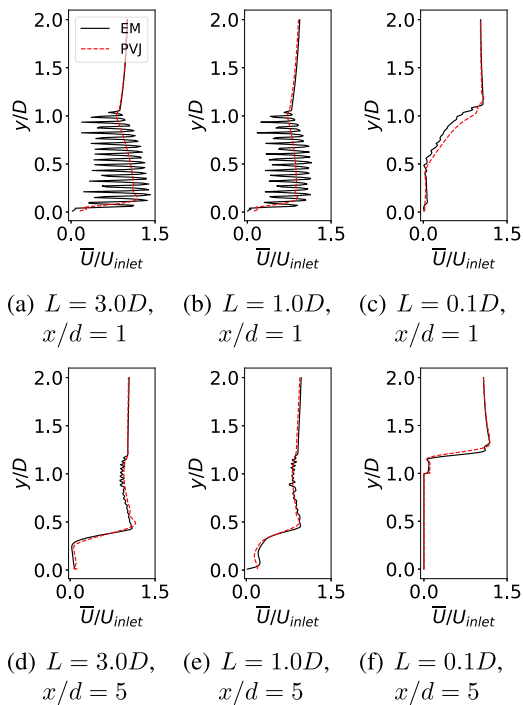


Fig. 9. Vertical profiles of time-averaged velocity magnitude,  $\bar{U}/U_{inlet}$ , downstream the B+45 barriers.

reported in Tables 1 and 2 (for the sake of simplicity, force coefficients are calculated also in this case based on the obstacle height).

### 5. Conclusions

In this paper, the accuracy of the PVJ approach as an alternative to the explicit modelling of permeable elements has been assessed for

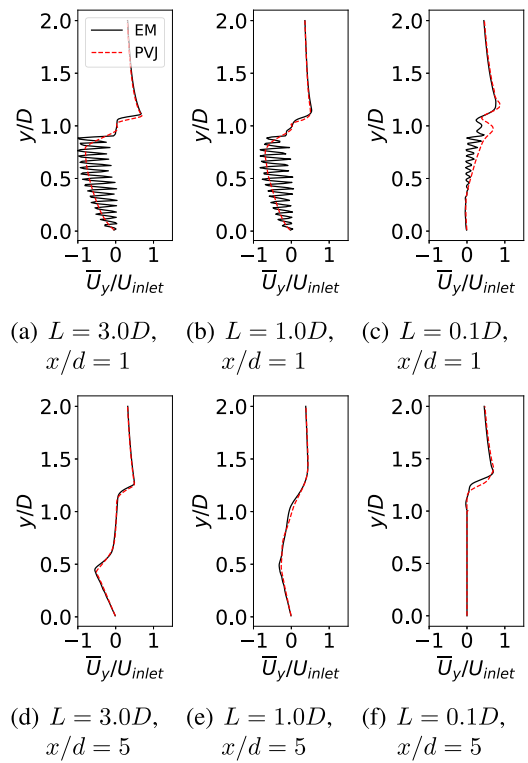


Fig. 10. Vertical profiles of time-averaged velocity component along the y-direction,  $\bar{U}_y/U_{inlet}$ , downstream the B-45 barriers.

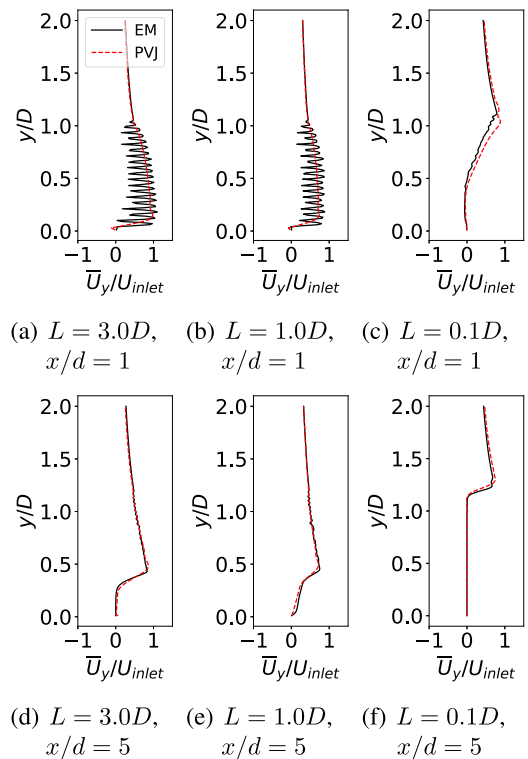


Fig. 11. Vertical profiles of time-averaged velocity component along the y-direction,  $\bar{U}_y/U_{inlet}$ , downstream the B+45 barriers.

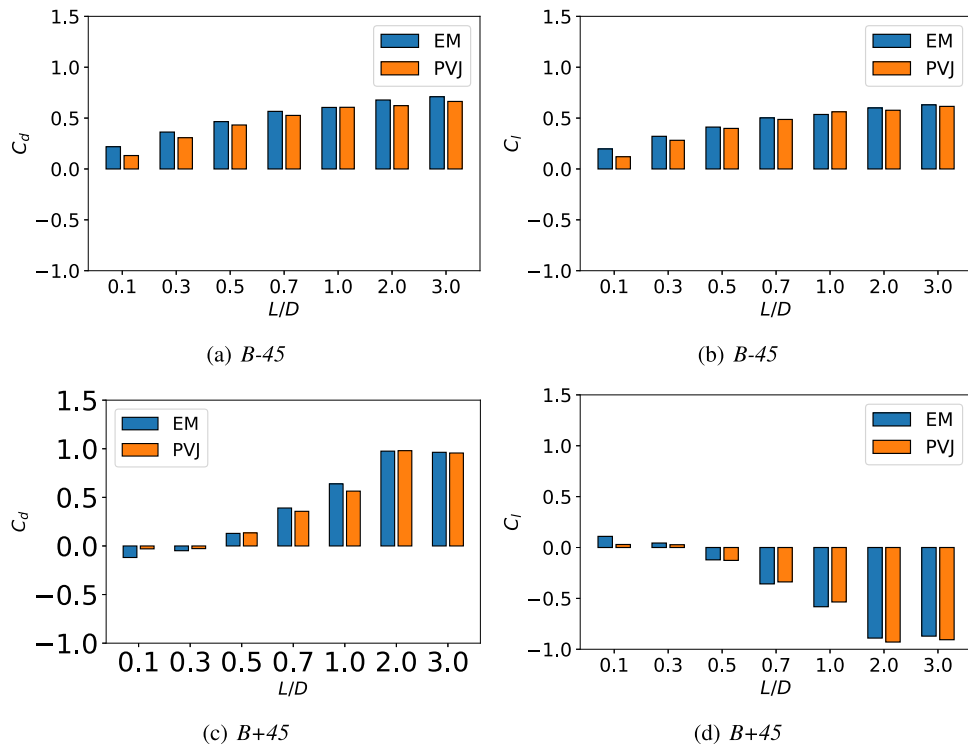


Fig. 12. Aerodynamic force coefficients measured on the lamellar screen.

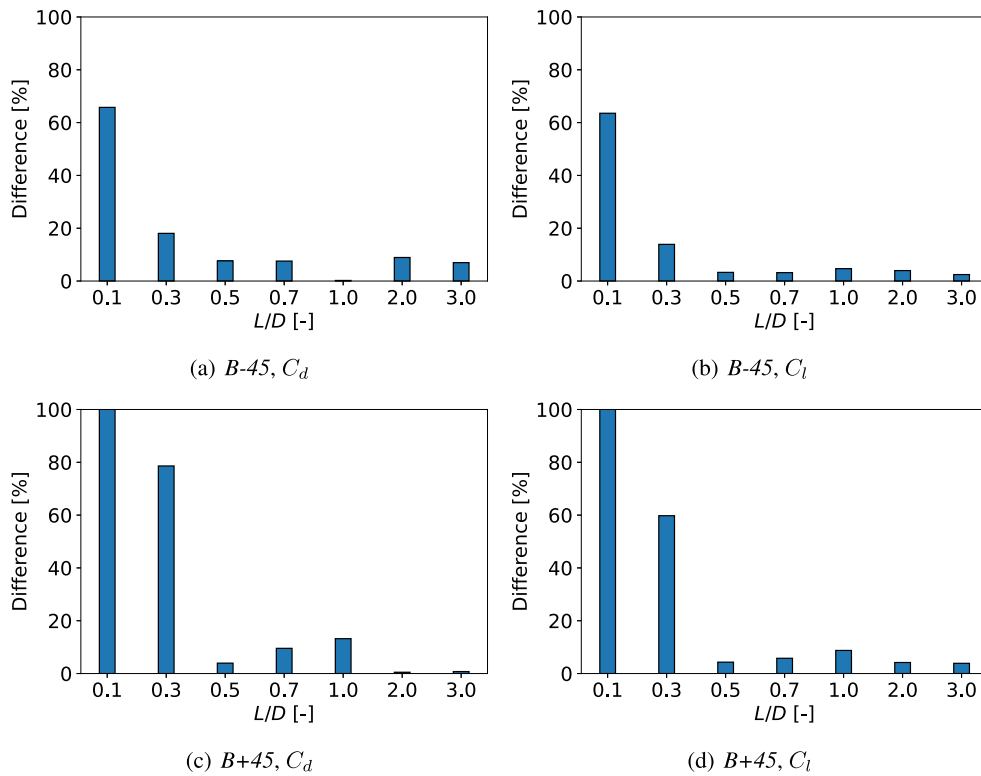


Fig. 13. The relative differences of aerodynamic coefficients measured on the lamellar screen.

the case of a lamellar screen upstream of a square and a rectangular obstacles. The approach is simple, straightforward to setup and can lead to substantial savings in terms of computational and set-up time.

Overall, good agreement is found between results obtained adopting EM and PVJ approaches. In particular, for all the studied cases, good

qualitative agreement is found, with PVJ always able to correctly capture the trends observed in the EM. In quantitative terms, differences between the two modelling approaches have been found to be in the order of 20% in the majority of the cases, with higher percent differences usually associated to small absolute values of the considered



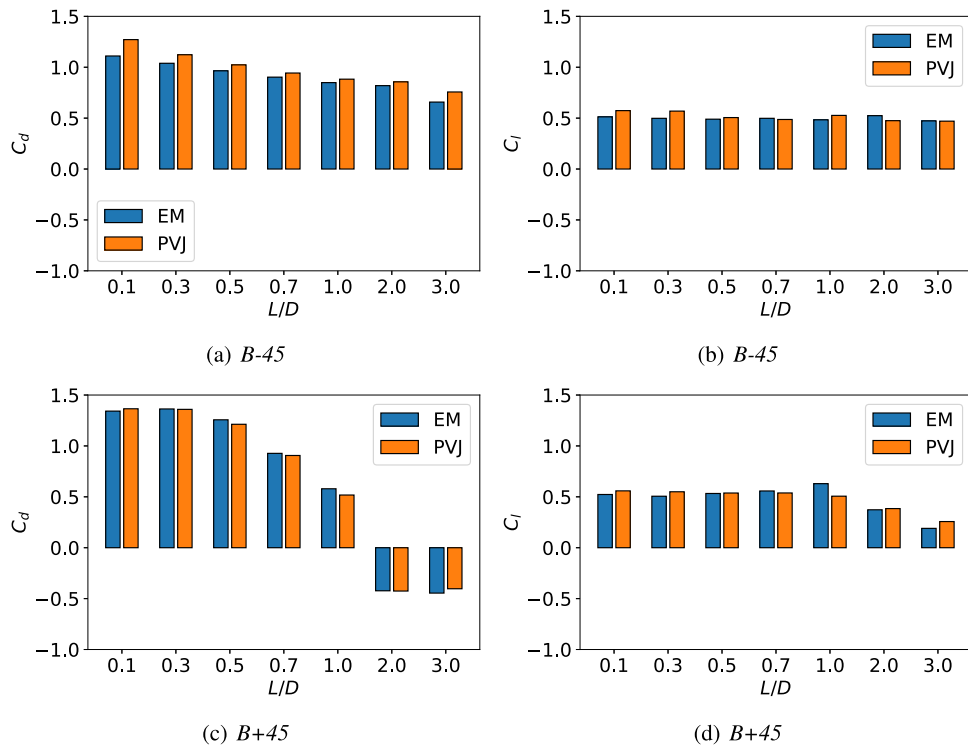


Fig. 14. The aerodynamic coefficients measured on the immersed obstacle.

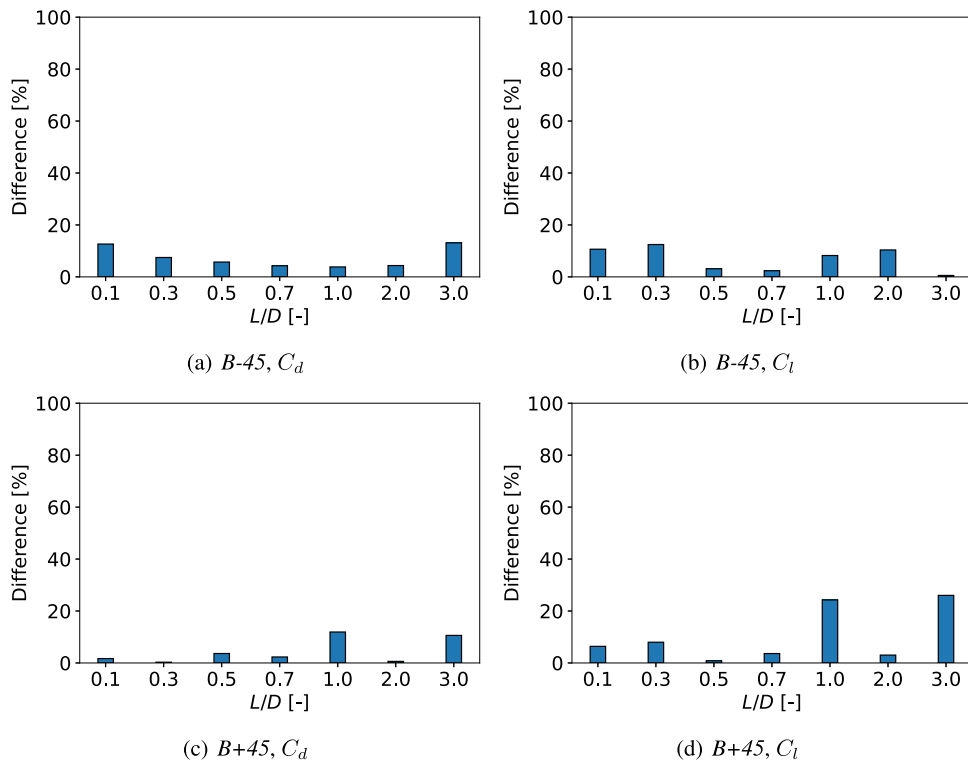


Fig. 15. The differences of aerodynamic coefficients measured on squares.

quantities. As expected, differences appear to be higher when a strong aerodynamic interaction is established between the lamellar screen and the obstacle immersed in its wake, i.e. for  $L/D \approx 1$ , which corresponds, for one of the analysed cases, to the case in which the flow downstream the lamellar screen impinges the obstacle right at the frontal corner.

In a summary, the proposed *PVJ* approach offers significant advantages in the modelling of permeable elements with respect to other homogenized approaches. In fact, contrarily to the classical pressure-jump approach, it is able to correctly capture flow deflections allowing for the modelling of lamellar screens and, contrarily to porous-media

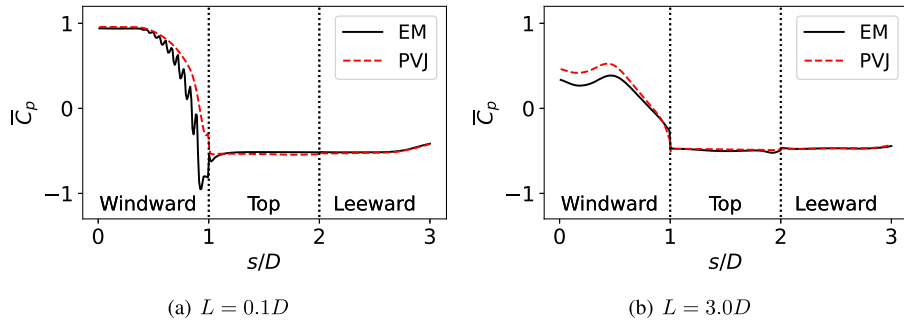


Fig. 16. Distribution of time-averaged pressure coefficient,  $\bar{C}_p$ , for the lamellar screen B-45.

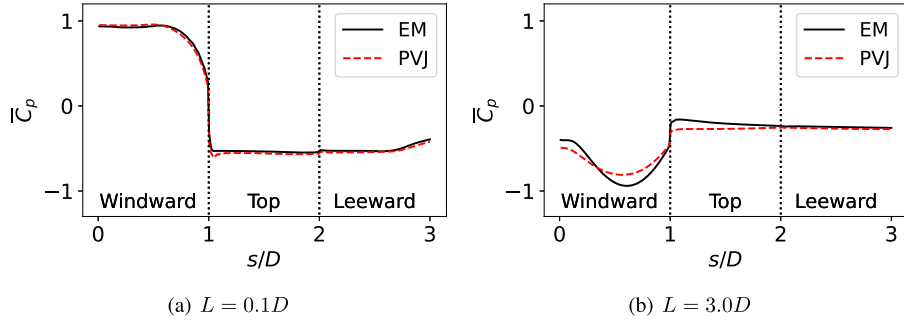


Fig. 17. Distribution of time-averaged pressure coefficient,  $\bar{C}_p$ , for the lamellar screen B+45.

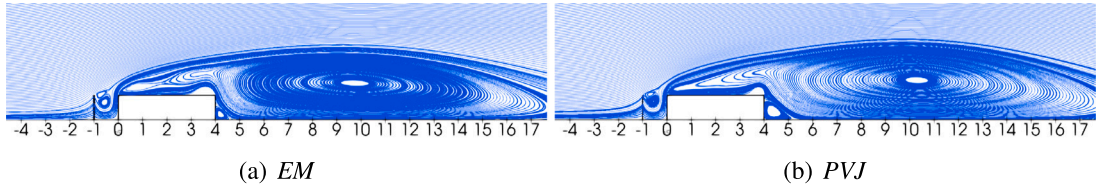


Fig. 18. Streamlines of the time-averaged velocity field for the B-45 barrier when  $L/D = 1.0$ .

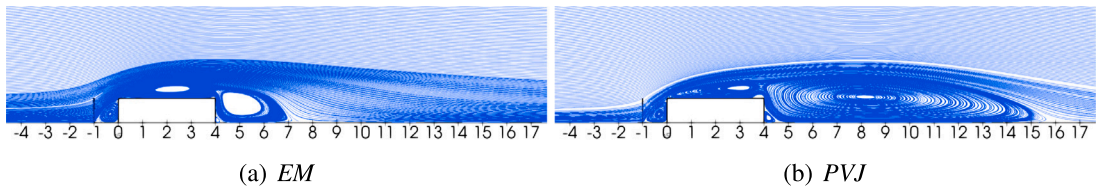


Fig. 19. Streamlines of the time-averaged velocity field for the B+45 barrier when  $L/D = 1.0$ .

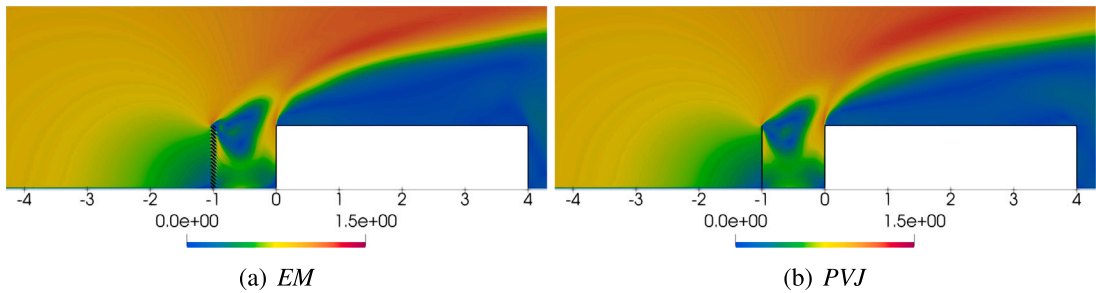


Fig. 20. Time-averaged velocity magnitude distribution,  $\bar{U}/U_{inlet}$ , for the B-45 barrier when  $L/D = 1.0$ .

models, it does not need to introduce a porous zone of very small thickness.

As a last note, we highlight that the present investigation using two-dimensional URANS shall not be extrapolated to other model

typologies. In particular, it is deemed necessary to repeat the same validation using scale-resolving turbulence models and, finally verify the accuracy of the obtained results with respect to experimental data. Despite such limitations, the present results clearly confirm that PVJ can

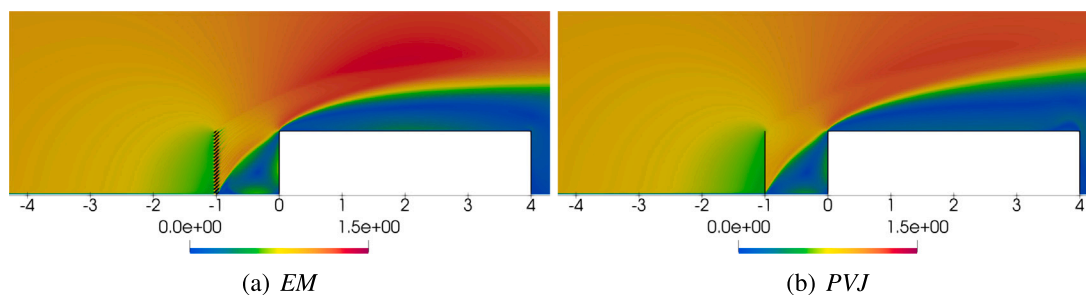


Fig. 21. Time-averaged velocity magnitude distribution,  $\bar{U}/U_{inlet}$ , for the B+45 barrier when  $L/D = 1.0$ .

Table 1

Force coefficients for the B-45 cases.

	$C_d$			$C_l$		
	EM	PVJ	Difference	EM	PVJ	Difference
Lamellar screen	0.62	0.57	8.1%	0.55	0.53	3.6%
Obstacle	0.84	0.88	4.8%	1.93	1.82	5.7%

Table 2

Force coefficients for the B+45 cases.

	$C_d$			$C_l$		
	EM	PVJ	Difference	EM	PVJ	Difference
Lamellar screen	0.65	0.59	9.2%	-0.59	-0.56	5.1%
Obstacle	0.41	0.37	9.8%	2.86	2.20	23.1%

be fruitfully used in two-dimensional URANS instead of cumbersome EM for the simulations of permeable surfaces.

#### CRedit authorship contribution statement

**Mao Xu:** Writing – original draft, Investigation. **Luca Patruno:** Writing – review & editing, Supervision, Conceptualization. **Stefano de Miranda:** Writing – review & editing, Supervision.

#### Declaration of competing interest

The authors declare that they have no known competing financial interests or personal relationships that could have appeared to influence the work reported in this paper.

#### Data availability

Data will be made available on request.

#### References

- Allori, D., Bartoli, G., Mannini, C., 2013. Wind tunnel tests on macro-porous structural elements: A scaling procedure. *J. Wind Eng. Ind. Aerodyn.* 123, 291–299.
- Azizi, F., 2019. On the pressure drop of fluids through woven screen meshes. *Chem. Eng. Sci.* 207, 464–478.
- Belloli, M., Rosa, L., Zasso, A., 2014. Wind loads and vortex shedding analysis on the effects of the porosity on a high slender tower. *J. Wind Eng. Ind. Aerodyn.* 126, 75–86.
- Bruno, L., Horvat, M., Raffaele, L., 2018. Windblown sand along railway infrastructures: A review of challenges and mitigation measures. *J. Wind Eng. Ind. Aerodyn.* 177, 340–365.
- Buljac, A., Kozmar, H., Pospíšil, S., Macháček, M., 2017. Flutter and galloping of cable-supported bridges with porous wind barriers. *J. Wind Eng. Ind. Aerodyn.* 171, 304–318.

- Darcy, H., 1856. *Les Fontaines Publiques De La Ville De Dijon: Exposition Et Application Des Principes À Suivre Et Des Formules À Employer Dans Les Questions De Distribution D'eau: ouvrage Terminé Par Un Appendice Relatif Aux Fournitures D'eau De Plusieurs Villes, Au Filtrage Des Eaux Et À La Fabrication Des Tuyaux De Fonte, De Plomb, De Tôle Et De Bitume.* Vol. 2, V. Dalmont.
- Eckert, B., Pfluger, F., 1942. *The Resistance Coefficient of Commercial Round Wire Grids.* Technical Report.
- Forchheimer, P., 1901. *Wasserbewegung durch boden.* Z. Ver. Deutsch. Ing. 45, 1782–1788.
- Jafari, M., Alipour, A., 2021. Review of approaches, opportunities, and future directions for improving aerodynamics of tall buildings with smart facades. *Sustainable Cities Soc.* 72, 102979.
- Kozmar, H., Procino, L., Borsani, A., Bartoli, G., 2014. Optimizing height porous wind barriers: porosity of roadway wind barriers for viaducts and bridges. *Eng. Struct.* 81, 49–61.
- Lo, Y.-L., Wu, Y.-T., Fu, C.-L., Yu, Y.-C., 2020. Wind load reduction effects on inner buildings by exterior porous façades. *Build. Environ.* 183, 107148.
- Menter, F.R., Kuntz, M., Langtry, R., 2003. Ten years of industrial experience with the SST turbulence model. *Turbul. Heat Mass Transf.* 4 (1), 625–632.
- Ooi, C., Chiu, P.-H., Raghavan, V., Wan, S., Poh, H.J., 2019. Porous media representation of louvers in building simulations for natural ventilation. *J. Build. Perform. Simul.* 12 (4), 494–503.
- Packwood, A., 2000. Flow through porous fences in thick boundary layers: comparisons between laboratory and numerical experiments. *J. Wind Eng. Ind. Aerodyn.* 88 (1), 75–90.
- Pomaranzi, G., Bistoni, O., Schito, P., Rosa, L., Zasso, A., 2021a. Wind effects on a permeable double skin façade, the ENI head office case study. *Fluids* 6 (11), 415.
- Pomaranzi, G., Bistoni, O., Schito, P., Zasso, A., 2021b. Numerical modelling of three-dimensional screens, treated as porous media. *Wind Struct.* 33 (5), 409–422.
- Raffaele, L., van Beeck, J., Bruno, L., 2021. Wind-sand tunnel testing of surface-mounted obstacles: Similarity requirements and a case study on a sand mitigation measure. *J. Wind Eng. Ind. Aerodyn.* 214, 104653.
- Taylor, G.I., 1944. *The aerodynamics of porous sheets.* Aeronaut. Res. Council. Rep. Memo. 2237, 163–176.
- Tominaga, Y., Shirzadi, M., 2022. RANS CFD modeling of the flow around a thin wind-break fence with various porosities: Validation using wind tunnel measurements. *J. Wind Eng. Ind. Aerodyn.* 230, 105176.
- Weller, H., 2012. Controlling the computational modes of the arbitrarily structured C grid. *Mon. Weather Rev.* 140 (10), 3220–3234.
- Wiegardt, K., 1953. On the resistance of screens. *Aeronaut. Q.* 4 (2), 186–192.
- Xu, M., Patruno, L., de Miranda, S., 2023. A pressure-velocity jump approach for the CFD modelling of permeable surfaces. *J. Wind Eng. Ind. Aerodyn.* 233, 105317.
- Xu, M., Patruno, L., Lo, Y.-L., de Miranda, S., 2020. On the use of the pressure jump approach for the simulation of separated external flows around porous structures: A forward facing step. *J. Wind Eng. Ind. Aerodyn.* 207, 104377.
- Xu, M., Patruno, L., Lo, Y.-L., de Miranda, S., 2022a. Simulation strategies for wind shields and porous barriers for bridge deck optimization. In: *Structures*. Vol. 40, 824–839.
- Xu, M., Patruno, L., Lo, Y.-L., de Miranda, S., Ubertini, F., 2022b. On the numerical simulation of perforated bluff-bodies: a cfd study on a hollow porous 5: 1 rectangular cylinder. *Wind Struct.* 34 (1), 1–14.
- Xu, M., Patruno, L., Lo, Y.-L., de Miranda, S., Ubertini, F., 2022c. Simulation of porous claddings using LES and URANS: A 5:1 rectangular cylinder. *Wind Struct.* 35 (1), 67–81.
- Zhou, J., Chen, Y., 2010. A review on applying ventilated double-skin facade to buildings in hot-summer and cold-winter zone in China. *Renew. Sustain. Energy Rev.* 14 (4), 1321–1328.